Precatalyst Evolution in PBiP-Pd Complexes for Electrocatalytic Proton Reduction

Hang Cao,† Yuka Aoyama,† Kristen Mast, Xiyuan Zhu, and Gongfang Hu*

Department of Chemistry, Colgate University, 13 Oak Drive, Hamilton, NY 13346, United States

Abstract

Main-group metals as supporting ligands for transition metals offer potential for bimetallic synergistic effects. We investigated a bismuth-palladium system utilizing a PBiP pincer ligand (**BiPd**^{Cl}) as precatalysts for electrocatalytic proton reduction with thiophenol. Rinse tests revealed the formation of a surface-bound active species, likely comprised of Pd-based heterogenous materials. NMR and UV-visible spectroscopic studies unveiled that in diluted solutions of polar coordinating solvents, the chloride *trans* to the bismuthane readily dissociates, affording the solvent-coordinated species (**BiPd**^{solvent}) as the predominant solution species. Following thiol–solvent ligand exchange, an equilibrium mixture of the solvent-bound species and the thiolate complex (**BiPd**^{S}) forms. The crystal structures of **BiPd**^{S} and an acetonitrile-coordinated model complex (**BiPd**^{AcN}) shows the thermodynamic *trans* influence of the bismuthane ligand. Structural analysis, corroborated by computational investigations, suggests that the reduction of **BiPd**^{solvent} is primarily ligand-based than Pd-centered, hinting at a Bi(III)–Pd(0) oxidation states rather than the Bi(I)–Pd(II) model suggested by the Lewis structure of **BiPd**^{solvent}. The electron-rich Pd and electron-poor Bi centers explain its electrochemical decomposition similar to other Pd(0) species. Our findings shed light on the electronic properties and reactivities of the studied Bi–Pd compounds, offering an example of ambiguous oxidation states within this system.

Synopsis

This study investigated a bismuth-palladium system as precatalysts for electrocatalytic proton reduction of thiophenol. Rinse tests indicate surface-bound active species formation. NMR and UV-visible studies reveal a predominant solvent-coordinated species in solution, with subsequent thiol–solvent ligand exchange leading to an equilibrium mixture with the thiolate complex. Structural analysis, backed by computational investigations, suggests that the reduction is more PBiP ligand-based rather than Pd-centered, suggesting a Bi(III)–Pd(0) oxidation-state assignment for the species in solution.

Introduction

Electrocatalysis has emerged as a powerful tool for addressing issues in energy sciences[1–3] and chemical synthesis.[4–7] Heterogeneous electrocatalysts offer greater potential for large-scale applications due to their long-term stability, while molecular electrocatalysts enable new reactivities through structural control and provide valuable insights into the underlying mechanisms.[8,9] Transition metal complexes with a single catalytic center remain mainstream in catalyst development. However, bimetallic systems are becoming increasingly attractive because of their potential synergistic effects, presenting advantages that cannot be readily achieved with individual metals.[10,11]

Compared to transition metals, main-group metals have received less attention in catalysis owing to their limited accessible redox transitions.[10–12] Nonetheless, a growing trend towards utilizing main-group metals in redox catalysis has become evident in the literature over the past decade. Two prominent research directions in this field include: (1) using a main-group metal as a supporting ligand for transition metals,[13–15] and (2) employing a main-group metal as the catalytic

center.[16–19] Both pathways have yielded promising results and provided valuable knowledge into harnessing main-group elements as catalysts. Investigations of metals in Group 13,[20] 14,[21] and 15[18,22] have revealed both similarities and differences between groups and periods.

Bismuth, the heaviest non-radioactive pnictogen, is notable for its low toxicity compared to other neighboring main-group metals. Recent studies by Cornella,[19,23,24] Dostál,[25–27] Gabbaï,[28] Gilliard,[29,30] Lichtenberg,[31–33] Limberg,[34–37] and many other research groups[38–42] have highlighted advancements in the synthesis, structural analysis, and catalytic properties of bismuth-containing species. The most stable oxidation state of Bi is +III, although crystal structures containing Bi(I) and Bi(II) have also been studied.[25,43,44] The presence of these accessible oxidation states resulting from single-electron transfers prompts us to consider the potential application of bismuth-based systems in electrocatalysis, where interfacial single-electron transfers to radical species are often involved.

When bismuth serves as a supporting ligand, determining its formal oxidation states becomes less straightforward and may depend on the geometry and the formal oxidation state of the transition metal center. In cases where crystal structures are unavailable or solution structures differ from those in the solid state, predicting the oxidation states of Bi and its associated transition metal can be challenging. In this study, we experimentally and computationally investigate a bimetallic palladium species with a PBiP pincer ligand, **BiPd**^{Cl} (Chart 1), originally prepared by Limberg and colleagues.[36] This compound yields solution species that electronically resemble a Bi(III)–Pd(0) motif rather than a Bi(I)–Pd(II) state. The compound functions as a precatalyst and decomposes into Pd-based heterogeneous materials, which are active for electrocatalytic proton reduction from thiophenol. Examinations of the transformation mechanism revealed ligand exchange reactions and a strong thermodynamic *trans* influence of the bismuthane ligand, as

evidenced by crystal structures and spectroscopic experiments in solution. The study highlights that probing the catalyst decomposition mechanism, although challenging due to the lack of well-defined structures, can contribute understanding into the divergent properties of solution and solid-state structures. This aspect remains underexplored for bimetallic main group–transition metal systems with strong intermetallic interactions.

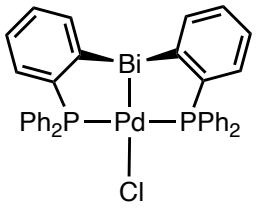

BiPd^{Cl}

Chart 1. The bimetallic bismuth-palladium complex studied here.

Results and Discussion

Electrochemical properties of BiPd^{Cl}. BiPd^{Cl} was synthesized based on Limberg's report.[36] The cyclic voltammogram of **BiPd**^{Cl} in *N*,*N*-dimethylformamide (DMF) exhibited an irreversible reduction feature at –1.85 V vs. the ferrocenium/ferrocene couple ($Fc^{+/0}$, Figure 1A). The Faradaic peak current (i_p, corrected for capacitive current) was measured at varying scan rates (ν) and showed a linear relationship with $\nu^{1/2}$, indicating that the reduction is under diffusion control. The diffusion coefficient was determined using the Randles–Ševčik equation (eq 1, see Supporting Information for the definition of symbols) to be 1.7×10^{-7} cm^2/s. This value is slightly larger than the values determined for Pd complexes using NMR spectroscopy.[45–47] The heterogeneous electron-transfer rate constant could not be determined by the Nicholson method[48] or Trumpet plot[49] due to the irreversibility of the reduction peak.

$$i_p = 0.4463nFAC\left(\frac{nF\upsilon D}{RT}\right)^{\frac{1}{2}} \qquad \text{(eq. 1)}$$

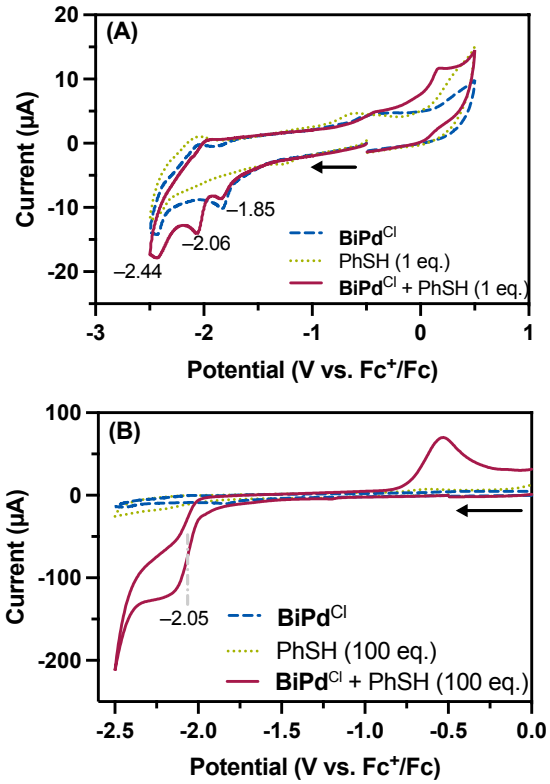

Figure 1. (A) Cyclic voltammograms of 0.5 mM **BiPd**^{Cl} in *N*,*N*-dimethylformamide (DMF) without acid (dashed line) and with the addition of 0.5 mM thiophenol (PhSH, solid). The dotted trace represents the voltammogram of 0.5 mM PhSH without **BiPd**^{Cl}. A new peak emerges at –2.06 V upon the addition of PhSH. (B) Cyclic voltammogram of 0.5 mM **BiPd**^{Cl} in DMF without acid (dashed) and with the addition of 50 mM PhSH (solid). The dotted trace represents the voltammogram of 50 mM PhSH without **BiPd**^{Cl}. The grey line indicates the position of $E_{cat/2}$, defined as the point at which the catalytic wave reaches half of its maximum current. The oxidation event around –0.5 V may arise from catalyst degradation and nanoparticle formation[50] (see text for details). All voltammograms were recorded under argon at 0.1 V/s in the presence of 0.1 M $[Bu_4N]^+[PF_6]^-$ as the supporting electrolyte. The experiments were conducted using a glassy carbon (3 mm diameter) working electrode, a Pt wire counter electrode, and a Ag/AgCl nonaqueous reference electrode. Applied voltage was corrected for ohmic drop determined through positive feedback experiments. All voltammograms were referenced to $Fc^{+/0}$ using a ferrocene internal reference at the end of each set of experiments. The black arrows below the curves indicate the starting point and the direction of scan.

We assigned this peak to a one-electron reduction event based on the internal-resistance-corrected peak width in the CV ($E_p - E_{p/2} = 55$ mV at 295 K, where E_p = is the peak potential, and $E_{p/2}$ is the potential where the current reaches half of the peak current) compared to that of the

equimolar ferrocene/ferrocenium couple (50 mV).[49] However, the current integration is much less than that of the equimolar ferrocene standard, indicating that only part of **BiPd**^{Cl} near the electrode surface is involved in this reduction. Titration using tetrabutylammonium chloride ($[Bu_4N]^+Cl^-$) had no impact on the reversibility of this peak, implying that the peak did not originate from reduction-induced chloride dissociation (Figure S1, Supporting Information). The wave did not gain reversibility with an increasing in the scan rate to 5 V/s (Figure S2). These results are consistent with an E_rC_i mechanism,[51] for which the rate constant of this ligand reorganization (k_d) can be estimated using the scan rate-dependent peak shift of the cathodic peak potential E_{pc} (eq 2). Since E_{redox} cannot be measured directly, we estimated it to be –1.86 V by assuming that at a low scan rate (0.1 V/s), the separation between E_{pc} and E_{redox} is 28.5 mV.[49] Using this assumption, the rate constant k_d is estimated to be 2.1×10^6 s^{-1}, which is consistent with a rapid ligand reorganization (Figure S3). Further studies indicated that at the concentration for electrochemical studies, the chloride has already departed from the coordination sphere upon dissolving **BiPd**^{Cl} in DMF, and this redox feature stems from the DMF-coordinated component, **BiPd**^{DMF}. As reduction-induced DMF dissociation in a DMF solution would result in a reversible peak, the irreversibility of the peak indicates possible reorganization of the bismuthane ligand.

$$E_{pc} = E_{redox} - 0.78\frac{RT}{F} + \frac{RT}{2F}\ln\left(\frac{RT}{F}\frac{k_d}{\upsilon}\right) \qquad \text{(eq. 2)}$$

Stoichiometric Reactions of BiPd^{Cl} with Thiophenol in DMF. Upon the addition of one equivalent of thiophenol (PhSH), the **BiPd**^{Cl} solution changed color from yellow to orange. In the cyclic voltammogram, a new irreversible reduction peak appeared at –2.06 V with a peak width of 60 mV (Figure 1A). UV-visible spectroscopy (UV-vis) also presented a peak shift from λ_{max} = 404 to 434 nm (Figure S4). These results revealed the transformation of **BiPd**^{Cl} to a new species upon reaction of thiophenol. Similar data analysis to the ones above gave estimated values for the

diffusion coefficient and the ligand-dissociation rate constant for this newly formed species to be 2.4×10^{-7} cm^2/s and 1.25×10^6 s^{-1}, respectively (Figure S5). Randles–Ševčik analysis also implies this new species freely diffused in solution. UV-vis titration using PhSH featured two isosbestic points (Figure 2A), indicating a reversible reaction between the solution form of **BiPd**^{Cl} and the newly formed species, without any intermediate exhibiting distinct absorption characteristics. Crystal structure showed this new species to be a thiolate complex and will be referred to as **BiPd**^{S} henceforth (*vide infra*). Titrating a **BiPd**^{Cl} solution containing three equivalents of PhSH using $[Bu_4N]^+Cl^-$ up to 100 equivalents showed no shift in the peak at 434 nm (Figure 2B). The reverse reaction from **BiPd**^{S} to **BiPd**^{Cl} can be accessed by titrating with HBF_4, which would form $[DMFH]^+[BF_4]^-$ in DMF.[52] Titration experiments reflect the fact that the equilibrium involves protons but not Cl^-, suggesting rapid chloride dissociation upon the initial dissolution of **BiPd**^{Cl}.

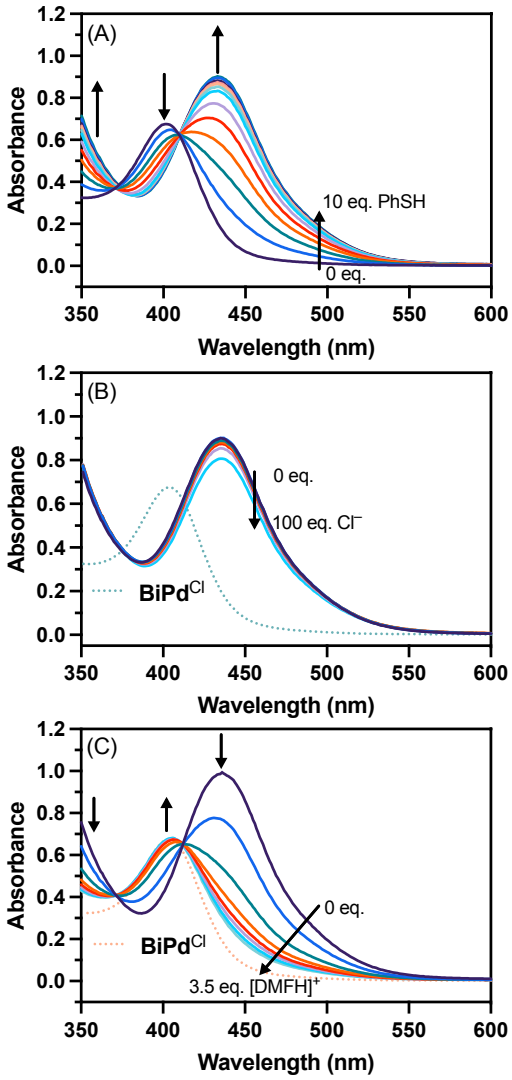

Figure 2. (A) UV-visible absorption spectra of a **BiPd**^{Cl} solution (0.15 mM) in anhydrous DMF titrated with 0 to 10 equiv of PhSH. Arrows indicate changes in the absorption profile, with λ_{max} shifted from 404 to 434 nm and showing two isosbestic points. (B) Titration of the solution of **BiPd**^{Cl} (0.15 mM) and PhSH (0.45 mM) with a $[Bu_4N]^+Cl^-$ solution up to 100 equiv relative to **BiPd**^{Cl}. No peak shift was observed; the decrease in absorbance resulted from sample dilution upon $[Bu_4N]^+Cl^-$ addition. The dotted line represents the absorption profile of **BiPd**^{Cl} at the same concentration for comparison. (C) Titration of a solution of **BiPd**^{Cl} (0.15 mM) and PhSH (0.45 mM) using a solution of $[DMFH]^+[BF_4]^-$ from 0 to 3.5 equiv, showing a shift in the peak from 434 nm back to 404 nm. The dotted line indicates the absorption profile of a **BiPd**^{Cl} solution at the same concentration for comparison. These spectra suggest that protons, rather than chloride, are involved in the equilibrium formation of **BiPd**^{S}.

Electrocatalytic Hydrogen-Evolution Reactions of BiPd^{Cl} with Thiophenol. We also discovered that continuous addition of thiophenol to a concentration of 50 mM (100 equiv) resulted in a catalytic current increase, with the onset potential at –1.75 V and $E_{cat/2}$ = –2.05 V (Figure 1B). Here, $E_{cat/2}$ represents the potential at which half of the maximum current is achieved. As $E_{cat/2}$ aligns with the peak potential of **BiPd**^{S}, the catalysis is presumed to arise from the reduction of **BiPd**^{S}. An oxidation event was observed at –0.5 V during the returning scan (Figure 1B), which may indicate decomposition of the precatalyst to heterogeneous species.[50] Although a current plateau was observed with 50 mM of PhSH, achieving the S-shaped curve under the pure kinetic condition (zone KS)[53,51] proved elusive, even with an increased scan rate up to 10 V/s or a higher amount of PhSH to 500 mM (1000 equiv, Figure S6). Controlled-potential electrolysis was conducted, followed by product analysis using gas chromatography. The only gas product detected in the headspace was H_2, produced with a Faradaic efficiency ~90% (Figure S7 and S8). Additionally, ^{1}H NMR spectra revealed the loss of the thiol proton (Figure S9), with no other sulfur-containing species detected.

The less-than-unity Faradaic efficiency and the oxidation peak observed in the anodic scan in Figure 1B suggest the decomposition of **BiPd**^{Cl} into heterogeneous species, likely Pd nanoparticles, under this condition. The decomposition is further confirmed through a rinse test: the working electrode was electrolyzed in a solution of **BiPd**^{Cl} and 50 mM thiophenol at –2.1 V for 15 min, rinsed with DMF, and transferred to a catalyst-free solution of 50 mM thiophenol. In this acid-only solution, similar catalytic response was observed, confirming that a catalytically active, electrode-bound material was generated (Figure 3C). This decomposition of precatalyst accounts for the sub-unity of Faradaic efficiency, as some charges are consumed during decomposition. Further control experiments using $Pd(PPh_3)_4$ instead of **BiPd**^{Cl} under the same

conditions also produced a surface-bound active species, evidencing that Pd nanoparticles likely play a role in the electrocatalysis (Figure S10). Electrocatalysis using sulfur-free proton sources, such as aniline hydrochloride and triethylamine hydrochloride, showed catalytic activity but also resulted in the decomposition of molecular species based on rinse tests. Changing the proton source to a mixture 3 equiv of thiophenol and excess ammonium salts, phenol, or water showed similar outcomes, with catalytic current increase and the formation of heterogeneous surface-bound species.

Reactions of BiPd^{Cl} Prior to Electroreduction. The decomposition of molecular precatalysts to heterogeneous active species has gained attention in recent years through rigorous electrochemical studies.[50,54–58] While the mechanism can be complex due to the lack of well-defined products, identifying potential intermediates can shed light on the reactivity of molecular systems. This understanding may inspire the design and exploration of future applications for the studied systems.

To understand the degradation pathways, it is essential to determine the reaction products formed from **BiPd**^{Cl} with PhSH. UV-vis titration unveiled no chloride involvement in the equilibrium formation of **BiPd**^{S} (Figure 2B). Therefore, it is likely that the Pd–Cl bond dissociates to form either the Pd–DMF complex **BiPd**^{DMF} or the solvent-free species **BiPd**$^{+}$ before reacting with thiol. The calculated redox potentials for **BiPd**^{DMF} and **BiPd**^{S} are consistent with experimental values by showing the same trend with a similar potential difference (Table S2). In contrast, **BiPd**^{Cl} displays a calculated redox potential similar to that of **BiPd**^{S}, which fails to explain the observed peak shift in CV (Figure 1A). This evidence supports that the solution structure differs from the solid-state structure of **BiPd**^{Cl}.

The reaction between **BiPd**^{Cl} and PhSH was monitored using ^{31}P NMR and UV-vis spectroscopy. Treating a 5 mM solution of **BiPd**^{Cl} in DMSO-d_6 (δ_P = 4.28 ppm) with an equimolar amount of PhSH produces a new peak (9.58 ppm), assigned to **BiPd**^{S}, consistent with observations from UV-vis studies (Figure S11). Increasing the PhSH concentration to 50 mM (10 equiv) accelerated the conversion (Figure S12). However, a third species at –6.90 ppm emerged after three hours, corresponding well with the chemical shift of free PPh_3 in DMSO-d_6. After 46 hours, the spectrum was dominated by a peak at 25.49 ppm, in line with the peak obtained from $Pd(PPh_3)_4$ in DMSO-d_6. These spectral changes illustrate that **BiPd**^{S} further reacts with excess PhSH to yield PPh_3 and possibly $Pd(PPh_3)_x$, species from $Pd(PPh_3)_4$ in solution.[59] Heating a sample containing **BiPd**^{Cl} and 10 equivalents of PhSH at 80 °C for one hour also formed a bismuth mirror, supporting the idea that Bi leaves the molecular motif in the presence of excess thiols (Figure S13). The thermal instability of **BiPd**^{Cl} and derivatives prevented us from determining rate constants using increased-temperature NMR experiments. The equilibrium constant for the formation of **BiPd**^{S}, determined using ^{31}P NMR spectroscopy in DMF, is 0.22 ± 0.07 (Figure S14 and Table S1).

Protons are necessary for the decomposition of **BiPd**^{Cl} into $Pd(PPh_3)_x$. We thus considered whether replacing PhSH with sodium thiophenolate (PhSNa) would afford **BiPd**^{S} while potentially slowing down any unwanted transformations, thereby facilitating the crystallization of **BiPd**^{S} on a larger scale. CV scans of **BiPd**^{Cl} with either equimolar thiophenol or sodium thiophenolate exhibited the same peak shift (Figure S16). ^{31}P NMR comparisons also affirm that protons are not necessary for the formation of **BiPd**^{S} (Figure S17). Chemical synthesis using **BiPd**^{Cl} and 5 equivalents of PhSNa in CH_2Cl_2 followed by crystallization afforded orange crystals of **BiPd**^{S} (Scheme 1), whose structure revealed a thiolate ligand binding to the Pd.

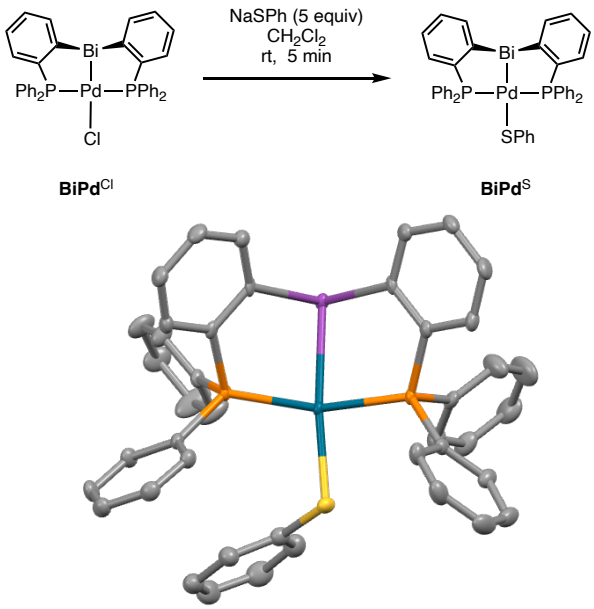

Scheme 1. Formation and the crystal structure of **BiPd**^{S}. The crystal structure is shown with 50% thermal ellipsoids. All hydrogen atoms are omitted for clarity. The absence of an anion in the crystal packing indicates the presence of a thiolate ligand rather than a thiol ligand binding to the Pd. Legend: carbon (gray), phosphorus (orange), bismuth (purple), palladium (blue green), and sulfur (yellow). Key structure parameters: $d_{Bi–Pd}$ = 2.6767(4) Å, $d_{Pd–S}$ = 2.3930(9) Å, $d_{Pd–P4}$ = 2.2787(8) Å, $d_{Pd–P5}$ = 2.2976(7) Å, ∠Bi–Pd–S = 172.52(2)°, ∠P4–Pd–P5 = 161.55(3)°, ∠Pd–Bi–C = 88.64(8)°, ∠Bi–Pd–P5 = 81.96(5)°. The geometry of Pd is approximately square planar, with the Houser's[60] τ_4 = 0.18. For **BiPd**^{Cl}, τ_4 = 0.16.[36]

The crystal structure of **BiPd**^{S} shows a slightly twisted square planar Pd geometry, indicative of a +II oxidation state in the solid form. The Pd–S bond length is 2.3930(9) Å, longer than many reported Pd(II)–SPh complexes found (2.30–2.36 Å)[61–64] in the Cambridge Crystal Data Center (CCDC), making it one of the longest Pd–thiolate bonds with an unbridged thiolate ligand. This Pd–S bond length aligns more closely with values measured for Pd(II)–thioether or μ-thiolatopalladium (II) complexes,[65–67] reflecting a weak Pd–S interaction and a strong thermodynamic *trans* influence of the bismuthane ligand. In contrast, the Bi–Pd interaction in **BiPd**^{S} is much shorter than in other reported systems, with a bond length at 2.6767(4) Å, slightly longer than the one reported for **BiPd**^{Cl} (2.646 Å).[36] For comparison, another Bi–Pd structure

prepared by the Limberg group containing a tetrahedral Pd(0) exhibits a Bi–Pd bond at 2.7342(11) Å and 2.7845(11) Å.[37] A PBiP–Pd(II) complex prepared by the Gabbaï group shows a Bi–Pd bond length at 2.9233(9) Å, with the Bi considered to be a σ-accepting, Z-type ligand.[28] Natural Bonding Orbital (NBO) analysis[68] can also shed light on the thermodynamic and kinetic *trans* effects of the bismuthane ligand. The PBiP ligand and the Pd–SPh motif were treated as separated units, and the dominant donor-acceptor interaction is Bi(6p) → σ*(Pd–S), stabilizing the Lewis structure with a deletion energy of 436.59 kcal/mol (Table S3). Chemical reduction of **BiPd**^{S} using potassium graphite resulted in no significant color change, and the resulting mixture of products did not form crystals or could be characterized by spectroscopy in our hands.

Investigations on the Species in Solution. The strong thermodynamic and kinetic *trans* effects of the bismuthane ligand are evidenced by (1) the crystal structure featuring a long Pd–S bond; (2) chloride dissociation upon the dissolution of **BiPd**^{Cl} at a low concentration; and (3) the formation of an equilibrium mixture between **BiPd**^{S} and **BiPd**^{DMF} or **BiPd**$^{+}$ in the absence of excess thiolate. These results highlight that the Pd center showed a weak affinity for anionic ligands such as chloride or thiolate. This behavior is unexpected for a relatively electron-poor, cationic Pd(II) center but can be better explained by considering a more electron-rich Pd center. To determine whether the complex exists as a solvent-coordinated species in solution, acetonitrile-coordinated **BiPd** derivatives were synthesized and crystallized (Scheme 2). Attempts to synthesize DMF-coordinated species in several ways afforded no crystals suitable for structural characterization (see Supporting Information). We used the acetonitrile complex **BiPd**^{AcN} as a model compound given the similar polarity of acetonitrile and DMF.

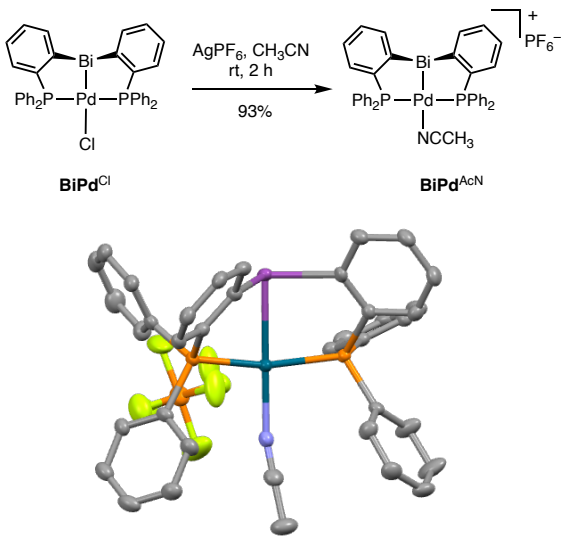

Scheme 2. Reaction of **BiPd** with $AgPF_6$ in acetonitrile and the structure of **BiPd**^{AcN}. The crystal structure is shown with 50% thermal ellipsoids. All hydrogen atoms are omitted for clarity. The asymmetric unit contains one non-coordinated CH_3CN molecule, which are also omitted for clarity. Legend: carbon (gray), phosphorus (orange), bismuth (purple), palladium (blue green), and nitrogen (light blue). Key structure parameters: $d_{Bi–Pd}$ = 2.6486(4) Å, $d_{Pd–N}$ = 2.142(3) Å, $d_{Pd–P3}$ = 2.3006(9) Å, $d_{Pd–P4}$ = 2.3200(9) Å, $d_{N–C}$ = 1.133(5) Å, ∠Bi–Pd–N = 177.84(9)°, ∠P3–Pd–P4 = 159.94(4)°, ∠Pd–Bi–C = 92.8(1)°, ∠Bi–Pd–P4 = 80.55(3)°. The geometry of Pd is approximately square planar, with the Houser's[60] τ_4 = 0.16.

The crystal structure of **BiPd**^{AcN} uncovers a weak bond between the Pd and the acetonitrile nitrogen (2.142(3) Å), a bond length significantly longer than 75% of crystal structures found in the CCDC database (1.886–2.094 Å). This bond length is comparable to those observed in structures with an aryl or vinyl ligand *trans* to the acetonitrile ligand.[69–73] The strong Bi–Pd interaction is showcased by the short Bi–Pd bond (2.6486(4) Å). These findings further underscore the strong thermodynamic *trans* influence of the bismuthane ligand. The ^{1}H NMR spectrum of the solution of **BiPd**^{AcN} in CD_2Cl_2 exhibited a peak corresponding to exclusively coordinated acetonitrile at 1.44 ppm (Figure S18 and Table S4). Upon addition of free CH_3CN to this solution, over 90% of the coordinated acetonitrile peak diminished, showcased by the new peak at 1.92 ppm corresponding to free acetonitrile. We therefore concluded that the coordinated acetonitrile of

BiPd^{AcN} rapidly exchange with the non-coordinated ones. One would expect the same rapid solvent ligand exchange in the case of **BiPd**^{DMF} in DMF.

Corroborative information was obtained from ^{31}P NMR analysis of **BiPd** species in various solvents. The ^{31}P chemical shifts of **BiPd**^{Cl} in different solvents at the same concentration (11 mM) and at room temperature are summarized in Table 1. Our measurement in C_6D_6 (6.04 ppm) and that reported by Limberg[36] (6.7 ppm) are more downfield compared to values from other solvents. In CD_2Cl_2, CD_3CN, and DMF, the **BiPd**^{Cl} solution exhibited ^{31}P signals at approximately the same position (~5.4 ppm). In DMSO-d_6, this peak shifts upfield to 4.68 ppm. These solvent-dependence shifts likely reflect composition changes influenced by varying solvent polarities. The ^{31}P peak for the **BiPd**^{AcN} was observed around 3.9 ppm. Based on the NMR comparison, we propose that in less coordinating and less polar solvents such as benzene, **BiPd**^{Cl} is the dominant species. As the solvent polarity increases, the proportion of **BiPd**^{Cl} also decreases, leading to the formation of **BiPd**^{solvent}. This mixture displays signals in the 4–6 ppm region. When chloride is completely removed chemically, the resulting solvent-bound species **BiPd**^{solvent}, affords signals around 3.9 ppm.

Table 1. ^{31}P NMR comparison of solutions of **BiPd**^{Cl} in various solvents ([**BiPd**^{Cl}]= 11 mM).

Solvent	δ_P (ppm)
C_6D_6	6.04
CD_2Cl_2	5.45
CD_3CN	5.45
DMF	5.41
DMSO-d_6	4.68
BiPd^{AcN} in CD_3CN	3.83
BiPd^{AcN} in CD_2Cl_2	3.87
BiPd^{AcN} in CD_2Cl_2 with CH_3CN	3.96

The chloride dissociation from **BiPd**^{Cl} is also concentration dependent, which suggests a dissociative mechanism. At lower concentrations used for UV-visible spectroscopy (0.15 mM) and

electrochemistry (0.5 mM), which are 20 to 100 times more diluted than the NMR samples, chloride dissociation becomes more pronounced, making **BiPd**^{solvent} the predominant species. This model aligns with the chloride-independent equilibrium between **BiPd**^{DMF} and **BiPd**^{S} from UV-vis titration (Figure 2) and the absence of redox features for **BiPd**^{Cl} in CV experiments.

A working hypothesis, depicted in Scheme 3, is proposed based on the experimental and computational findings. Additionally, a free energy landscape was constructed using density-functional theory (DFT) calculations at the level of ωB97X-D/Def2-SVP//ωB97X-D/Def2-QZVPP[74,75] (details provided in the Supporting Information). Structures of **BiPd**^{Cl}, **BiPd**^{S}, and **BiPd**^{DMF} optimized in solution (DMF) all exhibit an ion pair between Pd and the ligand trans to the bismuthane. Based on the dissociative ligand-exchange mechanism, a tricoordinated Pd species, **BiPd**$^{+}$, was proposed as the intermediate for this ligand exchange. Free-energy changes were calculated at various concentrations, revealing that the dissociation of the ligand *trans* to the bismuthane becomes more thermodynamically favorable as the concentration decreases. This observation aligns with equilibrium mixtures found in NMR samples (~10 mM), electrochemical samples (~1 mM), and the UV-vis titration samples (~0.1 mM). However, it remains unclear whether the conversion from **BiPd**$^{+}$ to **BiPd**^{S} is stepwise or concerted. UV-vis titration experiments suggest no intermediate buildup (Figure 2A), hinting at the fact that the coordination of thiol and proton transfer to DMF could be concerted if the S–H···O hydrogen bond was involved in facilitating the process. UV-vis titration **BiPd**^{Cl} in CH_2Cl_2 using PhSH indeed showed no formation of **BiPd**^{S}, as the solvent cannot serve as a proton acceptor (Figure S19).

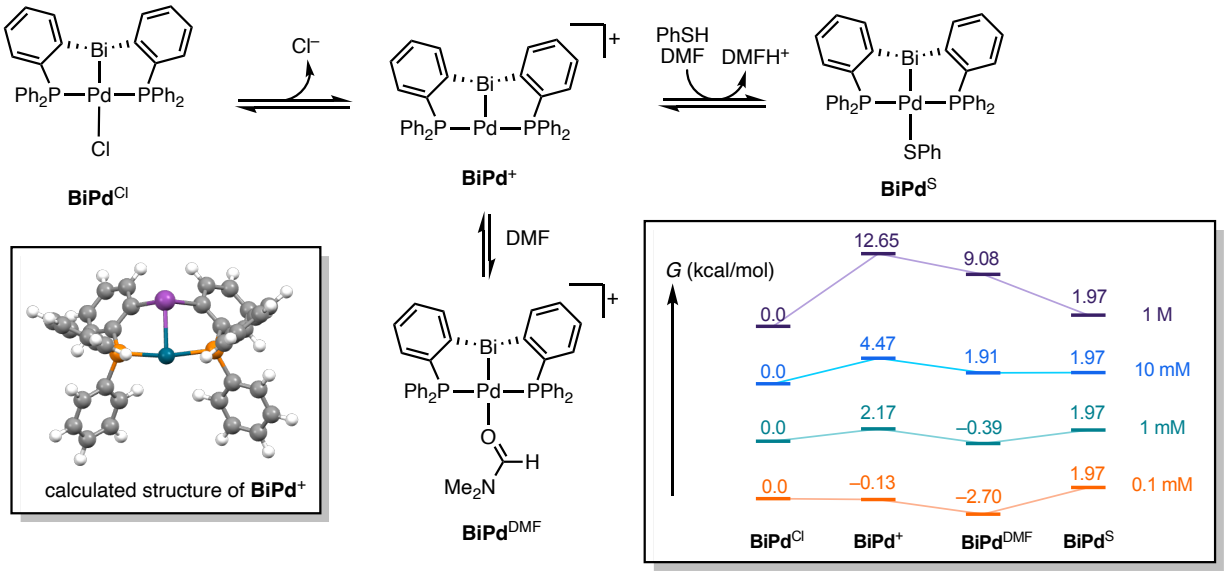

Scheme 3. Proposed solution transformations of **BiPd** complexes. The calculated structure of **BiPd**$^+$ is depicted in the left box. In the right box, the calculated reaction-free-energy changes (in kcal/mol) at various concentrations are plotted. As concentration decreases from the standard condition (1 M) to the concentrations of NMR samples (10 mM), electrochemistry samples (1 mM), and the UV-visible spectroscopic samples (0.1 mM), the dissociation of the ligand *trans* to the bismuthane becomes increasingly exergonic. Calculations utilized the ωB97X-D functional,[74] with the structure optimized with the Def2SVP basis and the single-point energies calculated with the Def2QZVPP basis.[76,77] All calculations were conducted using the SMD solvent correction in DMF.[78] Legend: carbon (gray), phosphorus (orange), bismuth (purple), palladium (blue green), and hydrogen (white).

Oxidation States of Bi and Pd. Efforts to obtain a crystal structure of **BiPd**$^+$ using $AgPF_6$ or NaB_{ArF} (B_{ArF} = tetrakis[3,5-bis(trifluoromethyl)phenyl]borate) in less coordinating solvents such as CH_2Cl_2 or chloroform were unsuccessful in our hands, leading to gradual darkening of the resulting species. We suspect that the **BiPd**$^+$ aggregates to form Pd black over time. DFT calculations provide insights into the electronic properties and the oxidation states of the Pd and Bi in **BiPd**$^+$. The optimized structure exhibited a tricoordinated Pd with a T-shaped geometry, with a Bi–Pd bond length of 2.680 Å (Scheme 3). NBO analysis uncovered a highly delocalized electronic configuration, with the Bi–Pd motif treated as a single unit. The Bi–Pd σ-bond formed

between the Bi 6p orbital (38%) and a Pd sd-hybridized[68] orbital (68%), more polarized toward Pd. Primary donor-acceptor interactions identified from deletion analysis included Bi(6s) → Pd(5p) and σ(Pd–P) → σ*(Bi–Pd), with deletion energy at 853.77 and 761.11 kcal/mol, respectively (Table S5). Significant contributions from the two interactions to the delocalization stability of the molecule indicate that its Lewis structure does not reflect the accurate electronic features (2.36% total non-Lewis contribution). The partially polarized Bi–Pd bond combined with the delocalization of the Bi 6s lone pair result in a +1.20 natural charge placed on Bi, while Pd bears a –0.015 charge. This Bi natural charge is close to that of $BiPh_3$ using the same method (+1.31). When coordinated with DMF or thiophenolate, the charges on Bi reduce to +1.06 and +0.92, respectively (Table S5). The more electrophilic nature of the Bi center and the more nucleophilic character of the Pd center support the formal oxidation state of Bi higher than +I in **BiPd**$^+$. One-electron reduction of **BiPd**$^+$ results in a neutral structure featuring a Bi–Pd bond at 2.802 Å, closer to the one found in Limberg's tetrahedral Pd(0)–Bi compound.[37] This reduced species could lead to decomposition, as observed in electrocatalytic studies, resembling other Pd(0) species.

Orbital analysis further shed light on the electronic properties of **BiPd**^{DMF} and its associated **BiPd**$^+$. As shown in Figure 3, the lowest-unoccupied molecular orbitals (LUMOs) of both compounds exhibit antibonding σ*(Bi–Pd) character, arising from interaction between the Bi 6*p* orbital and the Pd $5d_{x^2-y^2}$ orbital. σ*(Pd–P) also contributes significantly to these LUMOs, making them contain a greater component from the PBiP ligand. These results indicate that the reduction of **BiPd**^{DMF} or **BiPd**$^+$ is primarily ligand-based rather than Pd-centered, which would be expected from a Bi(III)–Pd(0) model but less so for a Bi(I)–Pd(II) motif. The highest occupied molecular orbitals (HOMOs) feature contributions from Bi, Pd, and the phosphine units, suggesting a highly delocalized electronic structure in these bimetallic complexes with strong

metal-metal interaction. Integrating observed reactivities with theoretical analysis, we suggest that **BiPd**^{solvent} and **BiPd**$^{+}$ are better described as a Bi(III)–Pd(0) motif, differing from Lewis structure-based assignments. Some tricoordinated Pd(0) structures have been studied experimentally before.[64,79] This ambiguity in oxidation-state assignment highlights that further investigation into associated structures and reactivity is essential for a comprehensive understanding of these Bi–Pd bimetallic systems.

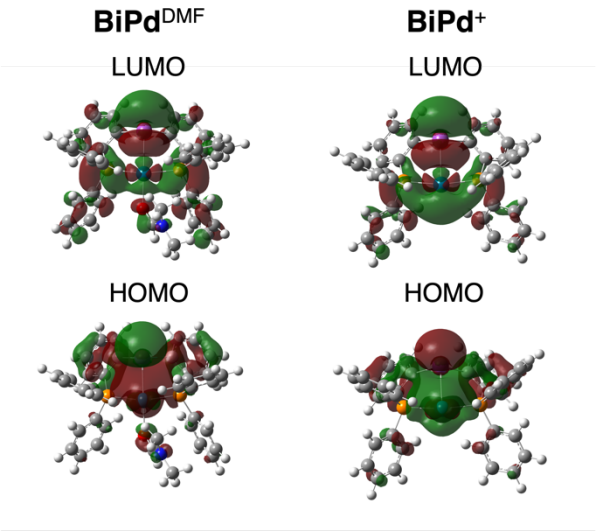

Figure 3. Highest occupied molecular orbitals (HOMOs) and lowest unoccupied molecular orbitals (LUMOs) of **BiPd**^{DMF} and **BiPd**$^{+}$. Both structures exhibit LUMOs composed of Bi 6p, Pd $5d_{x^2-y^2}$, and P 3p characters, with greater contribution from the PBiP ligand. Consequently, the one-electron reduction of the compounds are ligand-based events. The higher Bi component in the σ*(Bi–Pd) and the involvement of Pd $5d_{x^2-y^2}$ in bonding suggest an electron-rich Pd and an electron-poor Bi, supporting an oxidation model of Bi(III)–Pd(0) rather than the Bi(I)–Pd(II) model suggested by the Lewis structure.

Conclusions

In this investigation, we examined PBiP-pincer Pd complexes as precatalysts for the electrocatalytic reduction of protons from thiophenol and their transformations in solution. It was observed that under electrocatalytic conditions, the precatalyst decomposes into heterogeneous

materials active for hydrogen evolution reactions. In addition, crystal structure characterization of intermediates and spectroscopic studies revealed a strong thermodynamic and kinetic *trans* effects of the bismuthane ligand. In a diluted solution using a polar solvent such as DMF and acetonitrile, **BiPd**^{Cl} undergoes rapid ligand exchange, and the solvent-bound species **BiPd**^{solvent} is likely the dominant species, which will further react with thiol or thiolate to form **BiPd**^{S}. NBO and molecular orbital analysis suggested that in this solvent-coordinated structure, Bi is more electrophilic than Pd, with the oxidation states of Bi and Pd better described as +III and 0 instead of +I and +II, respectively. These findings help elucidate the reductive decomposition of the precatalyst, which is similar to other molecular Pd(0) species such as $Pd(PPh_3)_4$, and highlight the unique function of PBiP pincer ligand compared to other pnictogen based pincer ligands. The role of Bi as a supporting ligand for transition metals warrants further investigations and may lead to unconventional reactivity and catalytic applications.

Supporting Information

Experimental procedures and data are fully provided in the Supporting Information, including synthetic procedures, spectroscopic data, electrochemical experiments, crystallography data, and computational data (PDF). These files are available free of charge. Detailed crystallographic information is included in the CIF files published here or from the Cambridge Structure Database using CSD numbers 2352947 and 2352948. They are available free for charge at www.ccdc.cam.ac.uk/data_request/cif. All optimized structures for DFT calculations are available as .XYZ files provided along with this manuscript.

Author Contributions

†Hang Cao and Yuka Aoyama contributed equally. Hang Cao carried out quantitative electrochemical studies, rinse tests, and compound synthesis. Yuka Aoyama conducted intermediate synthesis, spectroscopic characterization and experiments, and crystallization. Kristen Mast conducted compound synthesis and preliminary cyclic voltammetry experiments. Xiyuan Zhu oversaw preliminary electrochemical studies and hydrogen gas detection. All crystallographic measurements and the corresponding data refinement along with computations were finished by Gongfang Hu. Project design, funding acquisition, administration, supervision, and oversight were done by Gongfang Hu. The original draft was written and edited by Gongfang Hu, with contributions from Hang Cao and other co-authors.

Conflicts of Interest

There are no conflicts to declare.

Acknowledgements

We kindly acknowledge Prof. Anthony Chianese and Prof. Jason Keith for fruitful discussions regarding this work. This work was supported by Colgate University Startup Fund. Computation resources were provided by Colgate University High-Performance and Research Computing Services.

Notes and References

(1) O'Mullane, A. P.; Escudero-Escribano, M.; Stephens, I. E. L.; Krischer, K. The Role of Electrocatalysis in a Sustainable Future: From Renewable Energy Conversion and Storage to Emerging Reactions. *ChemPhysChem* **2019**, *20* (22), 2900–2903. https://doi.org/10.1002/cphc.201901058.

(2) Masa, J.; Andronescu, C.; Schuhmann, W. Electrocatalysis as the Nexus for Sustainable Renewable Energy: The Gordian Knot of Activity, Stability, and Selectivity. *Angew. Chem. Int. Ed.* **2020**, *59* (36), 15298–15312. https://doi.org/10.1002/anie.202007672.

(3) Tang, C.; Zheng, Y.; Jaroniec, M.; Qiao, S.-Z. Electrocatalytic Refinery for Sustainable Production of Fuels and Chemicals. *Angew. Chem. Int. Ed.* **2021**, *60* (36), 19572–19590. https://doi.org/10.1002/anie.202101522.
(4) Francke, R.; Little, R. D. Redox Catalysis in Organic Electrosynthesis: Basic Principles and Recent Developments. *Chem. Soc. Rev.* **2014**, *43* (8), 2492. https://doi.org/10.1039/c3cs60464k.
(5) Yan, M.; Kawamata, Y.; Baran, P. S. Synthetic Organic Electrochemical Methods Since 2000: On the Verge of a Renaissance. *Chem. Rev.* **2017**, *117* (21), 13230–13319. https://doi.org/10.1021/acs.chemrev.7b00397.
(6) Moeller, K. D. Using Physical Organic Chemistry to Shape the Course of Electrochemical Reactions. *Chem. Rev.* **2018**, *118* (9), 4817–4833. https://doi.org/10.1021/acs.chemrev.7b00656.
(7) Malapit, C. A.; Prater, M. B.; Cabrera-Pardo, J. R.; Li, M.; Pham, T. D.; McFadden, T. P.; Blank, S.; Minteer, S. D. Advances on the Merger of Electrochemistry and Transition Metal Catalysis for Organic Synthesis. *Chem. Rev.* **2022**, *122* (3), 3180–3218. https://doi.org/10.1021/acs.chemrev.1c00614.
(8) Savéant, J.-M. Molecular Catalysis of Electrochemical Reactions. Mechanistic Aspects. *Chem. Rev.* **2008**, *108* (7), 2348–2378. https://doi.org/10.1021/cr068079z.
(9) Lee, K. J.; Elgrishi, N.; Kandemir, B.; Dempsey, J. L. Electrochemical and Spectroscopic Methods for Evaluating Molecular Electrocatalysts. *Nat. Rev. Chem.* **2017**, *1*, 0039. https://doi.org/10.1038/s41570-017-0039.
(10) Mankad, N. P. Selectivity Effects in Bimetallic Catalysis. *Chem. Eur. J.* **2016**, *22* (17), 5822–5829. https://doi.org/10.1002/chem.201505002.
(11) Campos, J. Bimetallic Cooperation across the Periodic Table. *Nat. Rev. Chem.* **2020**, *4* (12), 696–702. https://doi.org/10.1038/s41570-020-00226-5.
(12) Power, P. P. Main-Group Elements as Transition Metals. *Nature* **2010**, *463* (7278), 171–177. https://doi.org/10.1038/nature08634.
(13) You, D.; Gabbaï, F. P. Tunable σ-Accepting, Z-Type Ligands for Organometallic Catalysis. *Trends Chem.* **2019**, *1* (5), 485–496. https://doi.org/10.1016/j.trechm.2019.03.011.
(14) Takaya, J. Catalysis Using Transition Metal Complexes Featuring Main Group Metal and Metalloid Compounds as Supporting Ligands. *Chem. Sci.* **2021**, *12* (6), 1964–1981. https://doi.org/10.1039/D0SC04238B.
(15) Hollingsworth, W. M.; Hill, E. A. Exploring the Potential Role of Heavy Pnictogen Elements in Ligand Design for New Metal-Ligand Cooperative Chemistry. *J. Coord. Chem.* **2022**, *75* (11–14), 1436–1466. https://doi.org/10.1080/00958972.2022.2124863.
(16) Chu, T.; Nikonov, G. I. Oxidative Addition and Reductive Elimination at Main-Group Element Centers. *Chem. Rev.* **2018**, *118* (7), 3608–3680. https://doi.org/10.1021/acs.chemrev.7b00572.
(17) Lichtenberg, C. Main-Group Metal Complexes in Selective Bond Formations Through Radical Pathways. *Chem. Eur. J.* **2020**, *26* (44), 9674–9687. https://doi.org/10.1002/chem.202000194.
(18) Lipshultz, J. M.; Li, G.; Radosevich, A. T. Main Group Redox Catalysis of Organopnictogens: Vertical Periodic Trends and Emerging Opportunities in Group 15. *J. Am. Chem. Soc.* **2021**, *143* (4), 1699–1721. https://doi.org/10.1021/jacs.0c12816.
(19) Moon, H. W.; Cornella, J. Bismuth Redox Catalysis: An Emerging Main-Group Platform for Organic Synthesis. *ACS Catal.* **2022**, *12* (2), 1382–1393. https://doi.org/10.1021/acscatal.1c04897.
(20) Komuro, T.; Nakajima, Y.; Takaya, J.; Hashimoto, H. Recent Progress in Transition Metal Complexes Supported by Multidentate Ligands Featuring Group 13 and 14 Elements as Coordinating Atoms. *Coord. Chem. Rev.* **2022**, *473*, 214837. https://doi.org/10.1016/j.ccr.2022.214837.
(21) Kameo, H.; Nakazawa, H. Saturated Heavier Group 14 Compounds as σ-Electron-Acceptor (Z-Type) Ligands. *Chem. Rec.* **2017**, *17* (3), 268–286. https://doi.org/10.1002/tcr.201600061.
(22) Martínez, S.; Lichtenberg, C. Bismuth-Centered Radical Species: Access and Applications in Organic Synthesis. *Synlett* **2023**, a-2187-0455. https://doi.org/10.1055/a-2187-0455.

(23) Planas, O.; Wang, F.; Leutzsch, M.; Cornella, J. Fluorination of Arylboronic Esters Enabled by Bismuth Redox Catalysis. *Science* **2020**, *367* (6475), 313–317. https://doi.org/10.1126/science.aaz2258.
(24) Mato, M.; Spinnato, D.; Leutzsch, M.; Moon, H. W.; Reijerse, E. J.; Cornella, J. Bismuth Radical Catalysis in the Activation and Coupling of Redox-Active Electrophiles. *Nat. Chem.* **2023**, *15* (8), 1138–1145. https://doi.org/10.1038/s41557-023-01229-7.
(25) Šimon, P.; de Proft, F.; Jambor, R.; Růžička, A.; Dostál, L. Monomeric Organoantimony(I) and Organobismuth(I) Compounds Stabilized by an NCN Chelating Ligand: Syntheses and Structures. *Angew. Chem. Int. Ed.* **2010**, *49* (32), 5468–5471. https://doi.org/10.1002/anie.201002209.
(26) Vránová, I.; Alonso, M.; Lo, R.; Sedlák, R.; Jambor, R.; Růžička, A.; de Proft, F.; Hobza, P.; Dostál, L. From Dibismuthenes to Three- and Two-Coordinated Bismuthinidenes by Fine Ligand Tuning: Evidence for Aromatic BiC3N Rings through a Combined Experimental and Theoretical Study. *Chem. Eur. J.* **2015**, *21* (47), 16917–16928. https://doi.org/10.1002/chem.201502724.
(27) Dostál, L. Quest for Stable or Masked Pnictinidenes: Emerging and Exciting Class of Group 15 Compounds. *Coord. Chem. Rev.* **2017**, *353*, 142–158. https://doi.org/10.1016/j.ccr.2017.10.009.
(28) Lin, T.-P.; Ke, I.-S.; Gabbaï, F. P. σ-Accepting Properties of a Chlorobismuthine Ligand. *Angew. Chem. Int. Ed.* **2012**, *51* (20), 4985–4988. https://doi.org/10.1002/anie.201200854.
(29) Walley, J. E.; Warring, L. S.; Wang, G.; Dickie, D. A.; Pan, S.; Frenking, G.; Gilliard, Jr., R. J. Carbodicarbene Bismaalkene Cations: Unravelling the Complexities of Carbene versus Carbone in Heavy Pnictogen Chemistry. *Angew. Chem. Int. Ed.* **2021**, *60* (12), 6682–6690. https://doi.org/10.1002/anie.202014398.
(30) Warring, L. S.; Walley, J. E.; Dickie, D. A.; Tiznado, W.; Pan, S.; Gilliard, Jr., R. J. Lewis Superacidic Heavy Pnictaalkene Cations: Comparative Assessment of Carbodicarbene-Stibenium and Carbodicarbene-Bismuthenium Ions. *Inorg. Chem.* **2022**, *61* (46), 18640–18652. https://doi.org/10.1021/acs.inorgchem.2c03135.
(31) Ritschel, B.; Poater, J.; Dengel, H.; Bickelhaupt, F. M.; Lichtenberg, C. Double CH Activation of a Masked Cationic Bismuth Amide. *Angew. Chem. Int. Ed.* **2018**, *57* (14), 3825–3829. https://doi.org/10.1002/anie.201712725.
(32) Oberdorf, K.; Hanft, A.; Ramler, J.; Krummenacher, I.; Bickelhaupt, F. M.; Poater, J.; Lichtenberg, C. Bismuth Amides Mediate Facile and Highly Selective Pn–Pn Radical-Coupling Reactions (Pn=N, P, As). *Angew. Chem. Int. Ed.* **2021**, *60* (12), 6441–6445. https://doi.org/10.1002/anie.202015514.
(33) Heine, J.; Peerless, B.; Dehnen, S.; Lichtenberg, C. Charge Makes a Difference: Molecular Ionic Bismuth Compounds. *Angew. Chem. Int. Ed.* **2023**, *62* (24), e202218771. https://doi.org/10.1002/anie.202218771.
(34) Tschersich, C.; Limberg, C.; Roggan, S.; Herwig, C.; Ernsting, N.; Kovalenko, S.; Mebs, S. Gold– and Platinum–Bismuth Donor–Acceptor Interactions Supported by an Ambiphilic PBiP Pincer Ligand. *Angew. Chem. Int. Ed.* **2012**, *51* (20), 4989–4992. https://doi.org/10.1002/anie.201200848.
(35) Tschersich, C.; Braun, B.; Herwig, C.; Limberg, C. Coordination of Noble Metals by an Ambiphilic PBiP Pincer Ligand: Metallophilic Bi–Cu and Bi–Ag Interactions. *J. Organomet. Chem.* **2015**, *784*, 62–68. https://doi.org/10.1016/j.jorganchem.2014.09.019.
(36) Tschersich, C.; Braun, B.; Herwig, C.; Limberg, C. PBiP Pincer Complexes of Platinum, Palladium, and Iridium Featuring Metal–Metal Bonds Synthesized by Oxidative Addition of Bismuth–Halide Bonds. *Organometallics* **2015**, *34* (15), 3782–3787. https://doi.org/10.1021/acs.organomet.5b00439.
(37) Materne, K.; Braun-Cula, B.; Herwig, C.; Frank, N.; Limberg, C. Bismuthanes as Hemilabile Donors in an O_2-Activating Palladium(0) Complex. *Chem. Eur. J.* **2017**, *23* (49), 11797–11801. https://doi.org/10.1002/chem.201703489.
(38) Dikarev, E. V.; Gray, T. G.; Li, B. Heterobimetallic Main-Group–Transition-Metal Paddle-Wheel Carboxylates. *Angew. Chem. Int. Ed.* **2005**, *44* (11), 1721–1724. https://doi.org/10.1002/anie.200462433.

(39) Kindervater, M. B.; Marczenko, K. M.; Werner-Zwanziger, U.; Chitnis, S. S. A Redox-Confused Bismuth(I/III) Triamide with a T-Shaped Planar Ground State. *Angew. Chem. Int. Ed.* **2019**, *58* (23), 7850–7855. https://doi.org/10.1002/anie.201903354.
(40) Brannan, A. C.; Yoo, D.; Choi, J.; Lee, Y. Highly Distorted Bismuth–Nickel(II) Complex. *Inorg. Chem.* **2023**, *62* (22), 8589–8597. https://doi.org/10.1021/acs.inorgchem.3c00510.
(41) Chiappini, N. D.; Geunes, E. P.; Bodak, E. T.; Knowles, R. R. Organobismuth Compounds as Aryl Radical Precursors via Light-Driven Single-Electron Transfer. *ACS Catal.* **2024**, 2664–2670. https://doi.org/10.1021/acscatal.3c05598.
(42) Coburger, P.; Guilherme Buzanich, A.; Emmerling, F.; Abbenseth, J. Combining Geometric Constraint and Redox Non-Innocence within an Ambiphilic PBiP Pincer Ligand. *Chem. Sci.* **2024**, *15*, 6036–6043. https://doi.org/10.1039/D4SC00197D.
(43) Schwamm, R. J.; Harmer, J. R.; Lein, M.; Fitchett, C. M.; Granville, S.; Coles, M. P. Isolation and Characterization of a Bismuth(II) Radical. *Angew. Chem. Int. Ed.* **2015**, *54* (36), 10630–10633. https://doi.org/10.1002/anie.201504632.
(44) Ganesamoorthy, C.; Helling, C.; Wölper, C.; Frank, W.; Bill, E.; Cutsail III, G. E.; Schulz, S. From Stable Sb- and Bi-Centered Radicals to a Compound with a Ga=Sb Double Bond. *Nat. Commun.* **2018**, *9* (1), 87. https://doi.org/10.1038/s41467-017-02581-2.
(45) Guerrero, M.; Pons, J.; Branchadell, V.; Parella, T.; Solans, X.; Font-Bardia, M.; Ros, J. Synthesis and Characterization of Metallomacrocyclic Palladium(II) Complexes with New Hybrid Pyrazole Ligands. Diffusion NMR Studies and Theoretical Calculations. *Inorg. Chem.* **2008**, *47* (23), 11084–11094. https://doi.org/10.1021/ic8013915.
(46) Zuccaccia, C.; Bellachioma, G.; Ciancaleoni, G.; Macchioni, A.; Zuccaccia, D. Diffusion NMR Studies on Neutral and Cationic Square Planar Palladium(II) Complexes. *Inorganica Chim. Acta* **2010**, *363*, 595–600.
(47) Ananikov, V. P.; Zalesskiy, S. S.; Kachala, V. V.; Beletskaya, I. P. NMR Approach for the Identification of Dinuclear and Mononuclear Complexes: The First Detection of $[Pd(SPh)_2(PPh_3)_2]$ and $[Pd_2(SPh)_4(PPh_3)_2]$ - The Intermediate Complexes in the Catalytic Carbon-Sulfur Bond Formation Reaction. *J. Organomet. Chem.* **2011**, *696*, 400–405.
(48) Nicholson, R. S. Theory and Application of Cyclic Voltammetry for Measurement of Electrode Reaction Kinetics. *Anal. Chem.* **1965**, *37* (11), 1351–1355. https://doi.org/10.1021/ac60230a016.
(49) Savéant, J.-M.; Costentin, C. Single-Electron Transfer at an Electrode. In *Elements of Molecular and Biomolecular Electrochemistry*; John Wiley & Sons, Inc, 2019.
(50) Lee, K. J.; McCarthy, B. D.; Dempsey, J. L. On Decomposition, Degradation, and Voltammetric Deviation: The Electrochemist's Field Guide to Identifying Precatalyst Transformation. *Chem. Soc. Rev.* **2019**, *48* (11), 2927–2945. https://doi.org/10.1039/C8CS00851E.
(51) Saveánt, J.-M.; Costentin, C. Coupling of Electrode Electron Transfers with Homogeneous Chemical Reactions. In *Elements of Molecular and Biomolecular Electrochemistry*; John Wiley & Sons, Inc, 2019.
(52) Favier, I.; Duñach, E. New Protic Salts of Aprotic Polar Solvents. *Tetrahedron Lett.* **2004**, *45* (17), 3393–3395. https://doi.org/10.1016/j.tetlet.2004.03.025.
(53) Rountree, E. S.; McCarthy, B. D.; Eisenhart, T. T.; Dempsey, J. L. Evaluation of Homogeneous Electrocatalysts by Cyclic Voltammetry. *Inorg. Chem.* **2014**, *53* (19), 9983–10002. https://doi.org/10.1021/ic500658x.
(54) Anxolabéhère-Mallart, E.; Costentin, C.; Fournier, M.; Nowak, S.; Robert, M.; Savéant, J.-M. Boron-Capped Tris(glyoximato) Cobalt Clathrochelate as a Precursor for the Electrodeposition of Nanoparticles Catalyzing H_2 Evolution in Water. *J. Am. Chem. Soc.* **2012**, *134* (14), 6104–6107. https://doi.org/10.1021/ja301134e.
(55) Fang, M.; Engelhard, M. H.; Zhu, Z.; Helm, M. L.; Roberts, J. A. S. Electrodeposition from Acidic Solutions of Nickel Bis(benzenedithiolate) Produces a Hydrogen-Evolving Ni–S Film on Glassy Carbon. *ACS Catal.* **2014**, *4* (1), 90–98. https://doi.org/10.1021/cs400675u.

(56) Waldie, K. M.; Kim, S.-K.; Ingram, A. J.; Waymouth, R. M. Cyclopentadienyl Cobalt Complexes as Precatalysts for Electrocatalytic Hydrogen Evolution. *Eur. J. Inorg. Chem.* **2017**, *2017* (20), 2755–2761. https://doi.org/10.1002/ejic.201700188.
(57) Zheng, W.; Lee, L. Y. S. Metal–Organic Frameworks for Electrocatalysis: Catalyst or Precatalyst? *ACS Energy Lett.* **2021**, *6* (8), 2838–2843. https://doi.org/10.1021/acsenergylett.1c01350.
(58) Rooney, C. L.; Wu, Y.; Gallagher, D. J.; Wang, H. Restructuring and Integrity of Molecular Catalysts in Electrochemical CO_2 Reduction. *Nat. Sci.* **2022**, *2* (4), e20210628. https://doi.org/10.1002/ntls.20210628.
(59) Mann, B. E.; Musco, A. Phosphorus-31 Nuclear Magnetic Resonance Spectroscopic Characterisation of Tertiary Phosphine Palladium(0) Complexes: Evidence for 14-Electron Complexes in Solution. *J. Chem. Soc. Dalton Trans.* **1975**, No. 16–17, 1673–1677. https://doi.org/10.1039/DT9750001673.
(60) Yang, L.; Powell, D. R.; Houser, R. P. Structural Variation in Copper(I) Complexes with Pyridylmethylamide Ligands: Structural Analysis with a New Four-Coordinate Geometry Index, T4. *Dalton Trans.* **2007**, No. 9, 955–964. https://doi.org/10.1039/B617136B.
(61) Singhal, A.; Jain, V. K.; Varghese, B.; Tiekink, E. R. T. Synthesis and Characterisation of Mono- and Binuclear Palladium and Platinum Complexes with Organochalcogenides. *Inorganica Chim. Acta* **1999**, *285* (2), 190–196. https://doi.org/10.1016/S0020-1693(98)00335-1.
(62) Herrera-Álvarez, C.; Gómez-Benítez, V.; Redón, R.; García, J. J.; Hernández-Ortega, S.; Toscano, R. A.; Morales-Morales, D. [1,1′-Bis(diphenylphosphino)ferrocene]palladium(II) Complexes with Fluorinated Benzenethiolate Ligands: Examination of the Electronic Effects in the Solid State, Solution and in the Pd-Catalyzed Heck Reaction with the Catalytic System $[Pd(dppf)(SRF)_2]$. *J. Organomet. Chem.* **2004**, *689* (15), 2464–2472. https://doi.org/10.1016/j.jorganchem.2004.04.035.
(63) Kamiya, I.; Kawakami, J.; Yano, S.; Nomoto, A.; Ogawa, A. A Highly Regioselective Cyanothiolation of Alkynes via Oxidative Addition of Thiocyanates to Tetrakis(triphenylphosphine)palladium(0) Catalyst. *Organometallics* **2006**, *25* (15), 3562–3564. https://doi.org/10.1021/om0600442.
(64) Ma, Q.-Q.; Liu, T.; Li, S.; Zhang, J.; Chen, X.; Guan, H. Highly Efficient Reduction of Carbon Dioxide with a Borane Catalyzed by Bis(phosphinite) Pincer Ligated Palladium Thiolate Complexes. *Chem. Commun.* **2016**, *52* (99), 14262–14265. https://doi.org/10.1039/C6CC07987C.
(65) Rivera, G.; Bernès, S.; Barbarín, C. R. D.; Torrens, H. Heterobimetallic Platinum(II)–Palladium(II) Complexes Bridged by Fluorobenzenethiolates. Structure and Equilibria. *Inorganica Chim. Acta* **2009**, *362* (14), 5122–5125. https://doi.org/10.1016/j.ica.2009.07.036.
(66) Ulmann, P. A.; Mirkin, C. A.; DiPasquale, A. G.; Liable-Sands, L. M.; Rheingold, A. L. Reversible Ligand Pairing and Sorting Processes Leading to Heteroligated Palladium(II) Complexes with Hemilabile Ligands. *Organometallics* **2009**, *28* (4), 1068–1074. https://doi.org/10.1021/om801060m.
(67) Vivekananda, K. V.; Dey, S.; Maity, D. K.; Bhuvanesh, N.; Jain, V. K. Supramolecular Macrocyclic Pd(II) and Pt(II) Squares and Rectangles with Aryldithiolate Ligands and Their Excellent Catalytic Activity in Suzuki C–C Coupling Reaction. *Inorg. Chem.* **2015**, *54* (21), 10153–10162. https://doi.org/10.1021/acs.inorgchem.5b00806.
(68) Weinhold, F.; Carpenter, J. E. The Natural Bond Orbital Lewis Structure Concept for Molecules, Radicals, and Radical Ions. In *The Structure of Small Molecules and Ions*; Naaman, R., Vager, Z., Eds.; Springer US: Boston, MA, 1988; pp 227–236. https://doi.org/10.1007/978-1-4684-7424-4_24.
(69) Rauf, W.; Thompson, A. L.; Brown, J. M. Anilide Activation of Adjacent C–H Bonds in the Palladium-Catalysed Fujiwara–Moritani Reaction. *Dalton Trans.* **2010**, *39* (43), 10414–10421. https://doi.org/10.1039/C0DT00378F.
(70) Tsubomura, T.; Chiba, M.; Nagai, S.; Ishihira, M.; Matsumoto, K.; Tsukuda, T. Dinuclear Macrocyclic Palladium Complexes Having Pincer Coordinating Groups and Their Catalytic Properties in Mizoroki–Heck Reactions. *J. Organomet. Chem.* **2011**, *696* (23), 3657–3661. https://doi.org/10.1016/j.jorganchem.2011.08.024.

(71) Gupta, S. K.; Ghorai, D.; Choudhury, J. A New Type of Palladium-Pincer Complexes Generated via Hydrolytic Ring-Opening of Imidazole-2-ylidenes. *Organometallics* **2014**, *33* (12), 3215–3218. https://doi.org/10.1021/om500362x.
(72) Moriuchi, T.; Ohata, R.; Sakamoto, Y.; Hirao, T. Self-Assembly Properties of NCN Pincer Palladium(II) Complexes Bearing a Uracil Moiety. *Eur. J. Inorg. Chem.* **2014**, *2014* (27), 4626–4631. https://doi.org/10.1002/ejic.201400131.
(73) Ishikawa, Y.; Kimura, S.; Yamamoto, K.; Murahashi, T. Bridging Coordination of Vinylarenes to Pd_3- or Pd_4 Cluster Sites. *Chem Eur J* **2017**, *23* (57), 14149–14152. https://doi.org/10.1002/chem.201703023.
(74) Chai, J.-D.; Head-Gordon, M. Long-Range Corrected Hybrid Density Functionals with Damped Atom–Atom Dispersion Corrections. *Phys. Chem. Chem. Phys.* **2008**, *10* (44), 6615–6620. https://doi.org/10.1039/B810189B.
(75) Weigend, F. Accurate Coulomb-Fitting Basis Sets for H to Rn. *Phys. Chem. Chem. Phys.* **2006**, *8* (9), 1057–1065. https://doi.org/10.1039/B515623H.
(76) Weigend, F.; Ahlrichs, R. Balanced Basis Sets of Split Valence, Triple Zeta Valence and Quadruple Zeta Valence Quality for H to Rn: Design and Assessment of Accuracy. *Phys. Chem. Chem. Phys.* **2005**, *7* (18), 3297–3305. https://doi.org/10.1039/B508541A.
(77) Bursch, M.; Mewes, J.; Hansen, A.; Grimme, S. Best-Practice DFT Protocols for Basic Molecular Computational Chemistry. *Angew. Chem. Int. Ed.* **2022**, *61* (42). https://doi.org/10.1002/anie.202205735.
(78) Marenich, A. V.; Cramer, C. J.; Truhlar, D. G. Universal Solvation Model Based on Solute Electron Density and on a Continuum Model of the Solvent Defined by the Bulk Dielectric Constant and Atomic Surface Tensions. *J. Phys. Chem. B* **2009**, *113* (18), 6378–6396. https://doi.org/10.1021/jp810292n.
(79) Cui, P.; Wu, C.; Du, J.; Luo, G.; Huang, Z.; Zhou, S. Three-Coordinate Pd(0) with Rare-Earth Metalloligands: Synergetic CO Activation and Double P–C Bond Cleavage-Formation Reactions. *Inorg. Chem.* **2021**, *60* (13), 9688–9699. https://doi.org/10.1021/acs.inorgchem.1c00990.

For Table of Contents Only

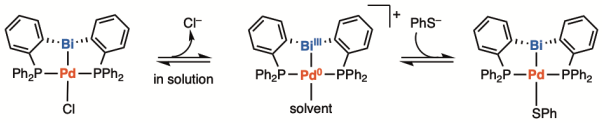

- Precatalyst for **electrocatalytic proton reduction** of thiolphenol
- Thermodynamic and kinetic **trans effects** of the PBiP ligand
- Likely **Bi(III)–Pd(0)** states in solution